CLOUD RADIATIVE FORCING DURING FIRE ACE DERIVED FROM AVHRR DATA

David R. Doelling
AS & M Inc.
Hampton, VA 23666

Patrick Minnis
Atmospheric Sciences
NASA-Langley Research Center
Hampton, VA 23681

Douglas A. Spangenberg, Venkatesan Chakrapani, Ashwin Mahesh
AS & M Inc.
Hampton, VA 23666

Shelley K. Pope, Francisco P. J. Valero
Center for Atmospheric Sciences
Scripps Institution of Oceanography
La Jolla, CA 92093

December 1999
Submitted to *FIRE ACE Special Issue*, *Journal of Geophysical Research*

Abstract

Cloud radiative forcing at the top of the atmosphere is derived from narrowband visible and infrared radiances from NOAA-12 and 14 Advanced Very High Resolution Radiometer (AVHRR) data taken over the Arctic Ocean during the First ISCCP Regional Experiment Arctic Cloud Experiment (FIRE ACE) during spring and summer of 1998. Shortwave and longwave fluxes were computed using narrowband-to-broadband conversion formulae based on coincident Earth Radiation Budget Experiment (ERBE) broadband and AVHRR narrowband radiances. The NOAA-12/14 broadband data were validated using model calculations and coincident broadband flux radiometer data from the Surface Heat Budget of the Arctic Ocean experiment and from aircraft data. The AVHRR top-of-atmosphere albedos agreed with the surface- and aircraft-based albedos to within $\pm$ 0.037 on an instantaneous basis. Mean differences ranged from –0.015 to 0.021 depending on the radiometer and platform. AVHRR-derived longwave fluxes differed from the aircraft- and surface-based fluxes by –0.1 to 0.5 Wm^{-2}, on average, when the atmospheric profiles were adjusted to force agreement between the observed and calculated downwelling fluxes. The standard deviations of the differences were less than 2%. Mean total albedo for the domain between 72°N and 80°N and between 150°W and 180°W changed from 0.695 in May to 0.509 during July, while the longwave flux increased from 218 to 229 Wm^{-2}. Net radiation increased from –90 to –2 Wm^{-2} for the same period. Net cloud forcing varied from –15.9 Wm^{-2} in May to –31.2 Wm^{-2} during July, while longwave cloud forcing was nearly constant between 7 and 10 Wm^{-2}. Shortwave cloud forcing dominated the cloud effect, ranging from –23 Wm^{-2} during May to –40 Wm^{-2} in July. The mean albedos and fluxes are consistent with previous measurements from the ERBE, except during May when the albedo is somewhat greater than the maximum ERBE value. The cloud forcing results, while similar to some earlier estimates are the most accurate to-date for regions in the Arctic. When no significant melting was present, the clear-sky longwave flux showed a diurnal variation similar to that over land under clear skies. The diurnal cycle became more like that over oceans when the surface albedo decreased because of widespread melting. These data should be valuable for understanding the Arctic energy budget and for constraining models of atmosphere and ocean processes in the Arctic.

1. INTRODUCTION

Clouds have a significant impact on the Arctic radiation budget. During winter, they produce a net warming effect at the surface by decreasing the amount of longwave radiation lost to space. This trapping effect may be counterbalanced during summer by clouds reflecting solar energy that would otherwise have warmed the surface. The change in the radiation balance due to clouds is termed radiative forcing. Estimates of cloud radiative forcing are sensitive to how well the cloudy and clear radiative fluxes are characterized because the forcing depends on the radiative properties of both the clouds and the surface. The similarities between clouds and snow-covered surfaces, both at solar and infrared wavelengths, as well as the large variability of the surface albedo make it a challenge to detect clouds using satellite data. Cloud radiative forcing, thus, is an uncertain quantity in the Arctic. Establishing its magnitude, sign, and seasonal variability is critical for assessing the role of clouds in the Arctic climate. The availability of a wide variety of surface, aircraft, and satellite measurements taken during the First ISCCP (International Satellite Cloud Climatology Project) Regional Experiment (FIRE) Arctic Clouds Experiment [ACE; *Curry et al.*, 1999] makes it possible to reduce the uncertainties in our estimates of cloud radiative effects in the Arctic.

The sensitivity of top-of-the-atmosphere (TOA) cloud radiative forcing (CRF) to measurements and to the cloud properties themselves is manifest in the variable estimates of its summertime values. Earth Radiation Budget Experiment (ERBE) broadband scanner data on National Ocean and Atmospheric Administration satellites, NOAA-9 & 10, were used to determine polar cloud CRF between 1985 and 1989 [e.g., *Harrison et al.* 1990]. Winter CRF over the Arctic is positive because the clouds are generally colder than the surface and no solar CRF can occur. *Harrison et al.* [1990] found negative CRF over the Arctic during July 1985 using a relatively crude method to detect cloud amounts in the ERBE 50-km footprints. This forcing ranged from –100 Wm^{-2} at 75°N to –5 Wm^{-2} at 90°N. *Curry and Ebert* [1992] computed the TOA CRF over the Arctic using climatologies of surface-observed cloud amounts and average in situ cloud microphysical properties adjusted to match ERBE fluxes. They also found substantial negative CRFs during summer at 80°N of ~-25, -45, and -70 Wm^{-2} during May, June, and July, respectively. *Rossow and Zhang* [1995] estimated a much smaller negative forcing of ~ -30Wm^{-2} during July at 80°N using ISCCP C2 cloud and surface properties in radiative transfer calculations. *Schweiger and Key* [1994] also computed CRF using ISCCP C2 products and found mean values of approximately –35, -55, and –60 Wm^{-2} during May, June, and July 1985-1989, respectively, for all ocean areas north of 62.5°N. Although new cloud retrievals are available from ISCCP [*Rossow and Schiffer* 1999], no CRF results have been published using the latest products. The newer ISCCP D2 datasets include additional cloud properties and show cloud amounts. Therefore, estimates of CRF using the new ISCCP products are expected to differ from the earlier values.

In this paper, a cloud amount dataset derived from Advanced Very High Resolution Radiometer (AVHRR) satellite imager data taken during FIRE ACE is used to provide a more accurate estimate of TOA cloud radiative forcing than heretofore possible. Because no satellite-based broadband radiation data were taken over the Arctic during FIRE ACE, empirical narrowband conversion methods are used to estimate broadband fluxes from the NOAA-12 and NOAA-14 AVHRR radiances. The derived fluxes are verified by comparisons to theoretical calculations and surface and aircraft radiation measurements. The results of these analyses provide a clearer picture of the role of clouds in the Arctic energy cycle and can serve as the basis for improved modeling of Arctic cloud and energy processes.

2. DATA & METHODOLOGY

a. Narrowband AVHRR data

Calibrated NOAA-12 and NOAA-14 AVHRR High-Resolution Picture Transmission (HRPT) 1-km images collected during FIRE ACE between 3 May and 31 July 1998 were used to compute narrowband visible (VIS; 0.65 µm) albedo and infrared (IR; 10.8 µm) equivalent blackbody temperatures [*Minnis et al.* 1999]. The pixel-level results for each of the 509 images were averaged on a 0.5° latitude by 2° longitude grid covering the area between 72°N to 80°N and 180°W to 150°W. This grid includes the varying position of the Surface Heat Budget of the Arctic Ocean (SHEBA) ship *Des Groseilliers* [*Perovich et al.*, 1999] that was initially centered near 76°N, 165°W. The images for each overpass do not always provide complete coverage of the domain, so there is incomplete sampling over the domain.

The VIS albedo α_v and IR temperature T for each pixel, accompanied by a scene classification of either clear or cloudy, were used to compute average values of cloud amount and the VIS albedos and IR temperatures for clear and cloudy conditions within each grid box [*Minnis et al.* 1999]. Also, for each image, the pixel-level values were averaged to obtain mean values for 25-km-radius circles centered on the *Des Groseilliers*.

A similar analysis was applied to NOAA-9 4-km AVHRR data taken during May, June, and July of 1986 over an area bounded by 65° and 75°N and 135° and 170°W. The NOAA-9 VIS reflectances were computed from the raw counts as in *Minnis et al.* [1993]. The VIS albedo, IR temperature, and cloud fraction were computed for each 2.5° latitude-longitude box in the 1986 domain following the methods of *Minnis et al.* [1999].

The IR temperatures were converted to IR fluxes using the approach of *Minnis et al.* [1991]. The narrowband flux is

$$M_{ir} = 6.18\, L_{ir}(0°), \qquad (1)$$

where the IR radiance at a viewing zenith angle of 0° is

$$L_{ir}(0°) = B(T) \,/\, \gamma(\theta). \qquad (2)$$

The Planck function at a wavelength of 10.8 µm is denoted by B and the limb-darkening function γ for viewing zenith angle θ is from *Minnis and Harrison* [1984].

b. ERBE data

The May-July 1986 2.5° latitude-longitude NOAA-9 ERBE [*Barkstrom et al.* 1989] shortwave (SW; 0.2 – 5.0 µm) albedos α_{sw} and longwave (LW; 5.0 – 50 µm) fluxes M_{lw}' were screened to eliminate viewing zenith angles greater than 45° and solar zenith angles exceeding

84° for the 1986 domain. These fluxes are coincident with the NOAA-9 AVHRR data. Due to calibration problems in the NOAA-9 ERBE LW fluxes, the values of the original fluxes M_{lw}' were corrected using the method of *Thomas et al.* [1995] to account for an earlier underestimation of LW flux. The values of LW flux used in this study are

$$M_{lw} = M_{lw}' - 0.020\, M_{sw}, \tag{3}$$

where M_{sw} is the shortwave flux and the coefficient of 0.020 is based on a nominal value of 1.78 spectral correction factor for polar snow and the mean correction factor slope of –0.036. This correction resulted in an average increase of 6 Wm^{-2} in the LW flux compared to the original AVHRR ERBE values. Because of the small differences between the clear and cloudy albedos, however, the effect of this correction on the LW cloud radiative forcing should be minimal. Some disagreement remains concerning the origin of this LW error. *Thomas et al.* [1995] ascribe it to an error in the ERBE SW channel. *R. N. Green* (personal communication, 1999) has concluded that the error is in the SW part of the ERBE total channel. Because of this uncertainty, no corrections are applied to the SW fluxes.

c. Other data

Temperature and humidity profiles taken near 0000, 0600, 1200, and 1800 UTC with rawinsondes launched from the *Des Groseilliers* were used to characterize the vertical atmospheric structure for the domain during FIRE ACE. These soundings were interpolated to the time of each overpass and are assumed to be representative of the entire domain. The National Center for Environmental Prediction (NCEP) 12-hourly gridded temperature and humidity analyses for 1986 were used for developing the infrared-to-longwave flux formula. These values were interpolated to the time of the NOAA-9 overpasses.

Broadband flux data were available from the National Center for Atmospheric Research C-130Q aircraft and the SHEBA ice camp [*Curry et al.* 1999]. The ice camp radiometers provided by the Atmospheric Radiation Measurement Program [ARM; see *Stokes and Schwartz*, 1994] were situated on a 10-m tower and consisted of up- and downwelling precision infrared radiometers and shortwave spectral pyranometers with a normal incidence pyrheliometer for direct beam broadband shortwave. The C-130Q was equipped with up- and downlooking NCAR-modified Eppley PSP pyranometers (0.285 – 2.80 µm) and NCAR-modified Eppley PIR pyrgeometers (3.5 to 50 µm). Details on the NCAR Eppleys and their attitude corrections can be found at http://www.atd.ucar.edu/dir_off/airborne and in *Bannehr and Glover* [1991]. It also included up- and downlooking Radiation Measurement System (RAMS) total broadband shortwave radiometers (TSBR; 0.224- 3.91 µm) and the infrared broadband radiometer (IRBR; 3.5 – 35 µm). Details of the RAMS instruments can be found in *Valero et al.* [1997]. All of the data were corrected for variations in aircraft attitude.

Only clear-sky surface radiometer data were used to compare with the satellite results. Radiative transfer calculations were used to adjust the surface measurements to the top of the atmosphere (TOA). A mean upwelling LW flux M_{LWS} at the SHEBA tower was computed for a half hour centered on the time of each satellite overpass during clear-skies. Temperature and humidity profiles were specified for the layer between the surface and 100 hPa using the nearest sounding, while the NCEP profiles of *Gupta et al.* [1995] provided temperatures and humidities for the upper atmosphere and the ozone concentrations for the entire atmosphere. These profiles were used in the model of *Fu and Liou* [1993] to compute the upwelling LW flux at the tower level and at the TOA. The surface skin temperature was varied in the model until the computed flux at the tower level matched the corresponding value of M_{LWS}. The computed LW flux at the TOA for this case is compared to the AVHRR-derived value. The SW surface albedo is computed from half hourly means of the up- and downwelling fluxes measured at the tower. These are used to specify surface albedo in the *Fu and Liou* [1993] model to compute the TOA albedo for each clear-sky AVHRR overpass.

The TOA SW albedos and LW fluxes were also computed using the model *Streamer* [*Key and Schweiger* 1998] to help estimate the uncertainties in the model calculations and input. The SHEBA soundings and NCEP analysis profiles were used to specify the temperature and humidity up to 100 hPa and above 100 hPa, respectively. Ozone concentrations for the entire atmosphere were taken from the NCEP profiles. The tower radiometers were used to specify the surface albedos for the SW calculations. The mean clear-sky radiative temperature from the satellite was used to specify the surface skin temperature for the LW calculations. It was assumed that atmospheric attenuation of the 10.8-µm radiances was insignificant in the clear Arctic skies and that the surface emissivity at 10.8 µm represented that of the entire LW spectrum.

The aircraft data were used when they were coincident with AVHRR overpasses and the C-130Q was in straight-line flight at a constant altitude. The highest altitude segments were selected to minimize the correction of the aircraft fluxes to the TOA. These altitudes ranged from 2.5 to 6.2 km. Data were used only if flight logs indicated clear skies above the aircraft and there was minimal variability in the aircraft attitude. Both May and July flights were used in the albedo comparisons, while only July Eppley PIR data were used for the LW comparisons because of technical problems with the PIRs during the May flights. To compare with the AVHRR results, mean fluxes were computed for flight segments centered on the AVHRR overpass time with a window of up to 30 min. Continuous segments were split into two or more data points if sudden changes in albedo occurred due to passage over a different scene type. The corresponding AVHRR pixel fluxes were averaged over a one-pixel-wide line coincident with the C-130Q flight path to match the aircraft fluxes.

To effect a direct comparison, it was necessary to adjust the aircraft fluxes to the TOA using radiative transfer calculations. To adjust the SW albedos, calculations were performed with the model of *Fu and Liou* [1993, hereafter FL] to compute a set of vertical profiles of albedos for each flight segment by specifying a range of surface albedos and the solar zenith angle. The soundings from either the SHEBA camp or Barrow, Alaska, depending on which was closest, were used to specify a vertical profile of temperature and humidity up to 100 hPa. Although these sites were sometimes hundreds of kilometers away from the aircraft, they were the closest weather stations. Temperatures and humidities for the upper atmosphere and the ozone concentrations for the entire atmosphere were specified using the profiles of *Gupta et al.* [1995]. A maritime aerosol optical depth of 0.1 was specified and distributed vertically according to the profiles of *Spinhirne* [1991].

The TOA albedo was determined by first matching the aircraft-measured albedo with the model-computed albedos at the flight altitude. Then the matching profile was followed to the TOA to obtain an estimate of α_{sw}. An example set of profiles is shown in figure 1 for May 4 for two solar zenith angles (SZA) noted by their cosines μ_o. The flight level is 6 km. If the aircraft-measured albedo is 0.57 at μ_o = 0.3, then the dashed curve would be followed to obtain an albedo of 0.55 at the TOA.

The LW TOA fluxes were estimated following a similar procedure except that the atmospheric profile was first adjusted prior to making the calculations. It was assumed that the calculated downwelling flux must match the observed downwelling radiation at the aircraft. This requirement was employed because the LW flux is more sensitive to atmospheric variations of temperature and humidity in the upper troposphere than the SW flux. Because the SHEBA sounding may not be representative of the profile at the aircraft location, the modeled downwelling flux was adjusted to match the aircraft value by altering the vertical profile of humidity above the aircraft. This was accomplished by modifying the relative humidity up to 100% in 10% increments from 200 hPa to flight altitude and in 5% increments between 100 and 200 hPa. In general, the relative humidity was increased to obtain more downwelling flux. Similarly, the surface skin temperature was adjusted until the calculated flux at flight altitude matched the observed upwelling value. In this fashion, it is ensured that the model calculations are consistent with the aircraft data. The resulting profiles used to obtain the flux matching are not necessarily the correct profiles. Many different corrections could have been used. The surface-temperature and humidity corrections were used because of their simplicity. The altered atmosphere and surface temperature were then used to compute the TOA LW flux. The results are compared to the satellite values.

d. Conversion to broadband albedos and fluxes

Narrowband radiance data have been successfully used to determine accurate mean broadband fluxes averaged over a period of time if the narrowband data are tuned to the particular instruments and region [*Minnis et al*, 1991; *Doelling et al.* 1998; *Valero et al.* 1999]. So far, no conversion algorithms have been specifically developed for the Arctic region. To obtain the broadband CRF, the broadband fluxes are computed from the AVHRR data using the regression formulae developed below using the approach of *Minnis and Smith* [1998].

The matched 1986 NOAA-9 ERBE and AVHRR albedos are shown in figure 2 with examples of several lines for constant SZA resulting from the regression equation:

$$\alpha_{sw} = 0.0293 + 0.7214\alpha_v + 0.0301\alpha_v^{\ 2} + 0.0869 \ln(1/\mu_o). \quad (4)$$

The squared correlation coefficient is 0.966 and the rms difference between the ERBE and AVHRR-predicted albedos is 0.0343 representing a relative error of 6.5%. The regression used 670 data points. The SW albedo for a given value of VIS albedo increases with SZA as seen by *Minnis and Smith* [1998] for a land surface.

Figure 3 shows the scatterplot and regression results for the matched IR and LW fluxes. The lines are from constant values of relative humidity RH above the altitude corresponding to the observed value of T. The LW flux is

$$M_{lw} = 66.56 + 7.6M_{ir} - 0.055M_{ir}^{2} - 0.247M_{ir} \ln(RH). \quad (5)$$

Values of RH for determining the regression fits were computed from the NCEP data as the column-weighted relative humidity (in percent) above the radiating surface. For consistency, RH was estimated during the FIRE ACE period from the SHEBA soundings using only the standard levels in the NCEP product. The squared correlation coefficient is 0.88 and the rms difference is 5.7 Wm^{-2}, a relative uncertainty of 2.5%. The regression used 615 data points. These regression fits are only valid for the subject domain during the summer months and are not necessarily applicable to other time periods or parts of the Arctic.

Equations (4) and (5) were applied separately to the gridded clear and cloudy AVHRR narrowband data taken during FIRE ACE to obtain SW and LW fluxes for all cloudy and clear pixels separately. Figure 4 shows an example of the results for an N12 image taken at 1936 UTC, 19 May 1998. Several extensive low cloud decks cover most of the scene with a large bright cloud-free strip along the center of the image. Despite the relatively thick cloud cover, the leads are visible through the clouds in the VIS image. Most of the clouds have a lower reflectance than the adjacent clear areas. After correcting for bidirectional reflectance differences, however, the SW albedos of the clear areas are slightly less than the nearby cloudy areas. Cloud edges on the eastern and southern sides of the oval-shaped cloud deck in the lower left corner are brighter than the interior. The northern and western edges are much darker than the deck's interior. Clear areas adjacent to the northern and western edges are in shadow and are the darkest parts of the scene. Although warmer than the lower clouds to the east and north, this oval cloud mass apparently is much thicker because it shows the edge effects. The extreme effects to due the cloud geometry are not taken into account with the anisotropic bidirectional reflectance models.

e. Cloud forcing

The standard definitions of LW, SW, and net CRF are, respectively,

$$\text{LWCRF} = M_{lw}(\text{CLR}) - M_{lw};$$

$$\text{SWCRF} = S[\alpha_{SW}(\text{CLR}) - \alpha_{SW}];$$

and

$$\text{NETCRF} = \text{LWCRF} + \text{SWCRF},$$

where S is the mean incoming solar flux and CLR refers to the clear-sky condition. The instantaneous measured fluxes were interpolated to every local hour using ERBE time-space averaging techniques [*Young et. al.* 1998] to minimize the effects of the AVHRR sampling patterns. The resulting fluxes were used to compute hourly CF parameters as well as the net flux,

$$M_{net} = S(1- \alpha_{SW}) - M_{lw}.$$

All of the parameters were then averaged over all hours to determine monthly means and monthly hourly means. The albedos were averaged using μ_o-weighting.

3. RESULTS

a. Flux distributions

The clear-sky products only used measurements for which the instantaneous clear amounts are greater than 10%. This is necessary to minimize shadow or three-dimensional cloud effects due to the high solar zenith angles. Figure 5 shows the mean clear-sky and total albedos for each of the months. During May, the clear-sky albedos range from 0.61 in the south to 0.70 at the northern edge of the domain. All of the albedos drop dramatically during June resulting in a south-to-north variation between 0.46 and 0.59. Ponds began to appear on the ice near the SHEBA camp around the beginning of June. The diminished clear-sky albedos during June are consistent with ponding and a breakup of the ice pack in the south. By the end of July, the clear-sky albedos have dropped another tenth resulting in a range from 0.35 along the southern edges to 0.50 in the north. Significant areas of nearly ice-free water occurred along the southern boundary of the domain. The addition of clouds yields total albedos that are greater in all cases, varying from 0.66 to 0.72 during May down to a range of 0.42 to 0.60 during July.

The clear LW fluxes are characterized by a 14 Wm^{-2} north-south gradient during May that is replaced by a less variable flux during June as the surface heats up (figure 6). During July, the surface is warmer still, with only a 5 Wm^{-2} north-south gradient. The total LW flux reflects the presence of colder clouds because it drops at all locations. The gradient in M_{lw} is generally north-to-south, except during June when the cloud gradient is from east-to-west [*Minnis et al.* 1999]. During July, the SHEBA camp is located in an area with the maximum cloud cover and, hence, is near the minimum in M_{lw}.

Differences in the clear and total albedos and fluxes are more easily seen in the CRF distributions in figure 7. SWCRF varies from -10 to -35 Wm^{-2} during May. As the surface albedo decreases, the SW cloud forcing increases during June and July to values between -25 and -65 Wm^{-2}. The greatest SWCRF occurs during July near the ship. The changes in LWCRF are less dramatic. North of the ship, LWCRF barely rises above zero reflecting the dominance of low clouds in that area. LWCRF varies from 3 to 16 Wm^{-2} during May and July. The gradients reverse from May to July with low relatively warm clouds dominating in southern part of the domain during the latter period. The net forcing is negative during all 3 months indicating that the clouds are tempering the warming of the Arctic during the summertime. Because the SW forcing is considerably larger in magnitude than the LW forcing, the distributions of NETCRF are similar to the SWCRF patterns. As a result of cloud cover, the radiative energy in the northern part of the domain is reduced by up to 50 Wm^{-2} during July. In May, the overall cloud effect is much smaller, ranging from -5 to -27 Wm^{-2}.

Table 1 summarizes the AVHRR-based monthly mean radiation results for the entire domain. The total albedos are greater than the clear albedos in the FIRE ACE domain by an average of 0.065 to 0.077. Accounting for the cloud amounts and the difference between the total and clear albedos, it was determined that the cloudy sky albedos are 0.709, 0.619, and 0.548, during May, June, and July, respectively. Thus, the cloudy-sky albedos are 0.066 to 0.125 greater than the clear albedos. The albedo differences translate to SWCRF differences of -23 to -40.3 Wm^{-2}. The mean LW fluxes increase for both total and clear conditions as the season progresses with the cloudy-sky LW fluxes ranging from 214.1 Wm^{-2} in May to 224.8 Wm^{-2} in July. The overall LWCRF remains low during the entire period between 7 and 10 Wm^{-2}. The net flux is strongly negative during May but is almost nil by the end of July for the total sky case. With the onset of melting during June, the clear-sky net radiation increases by almost 80 Wm^{-2} from May through June becoming significantly positive by July. This increase in absorbed solar energy produces only a 10-12 Wm^{-2} increase in clear LW flux suggesting, in the absence of any net advective effects, that much of the absorbed solar energy was used in melting ice and evaporating water. The clouds reduced the net warming of the system by 16 to 31 Wm^{-2} producing a negative mean net flux for all conditions throughout the FIRE ACE period considered here.

Diurnal variations of these parameters were also computed using the hourly means. Figure 8 shows the albedos as a function of local time for each month with the mean hourly values of μ_o. The clear-sky albedos are relatively flat with variations of less than 0.03 over a given day. Total sky albedo is more variable with minima occurring shortly after local noon and maxima near local midnight when μo ranges from 0.09 to 0.16 during the period. The total albedo variation shows the impact of the of clouds which generally become more reflective with decreasing μ_o. The LW fluxes in figure 9 have less variability with a maximum mean diurnal range that is less than 4 Wm^{-2} during all months. Some of the diurnal variability is due to the clear-sky LW fluxes increasing to a maximum shortly before local noon. However, the total flux diurnal range equals or exceeds the clear-sky values during all 3 months suggesting a consistent diurnal variation in the clouds. Minnis et al. [1999] found that the cloud cover peaked shortly before noon during all 3 months. To obtain a relative maximum in total LW flux near local noon that equals or exceeds the clear-sky value, the mean cloud cover occurring during the late morning to mid-afternoon must have frequently been warmer than the surface, especially during May and June. *Minnis et al.* [1999] found that the frequency of elevated inversions decreased from 90% to 30% from May to July. The diurnally dependent occurrence of clouds in such inversion layers could help explain the diurnal variations seen in figure 9. Additionally, the clouds may have been thin enough so that surface warming occurred and was detectable through the clouds or the difference between the clear and total LW flux diurnal cycles may be an artifact of the data processing. The averaging process assumed that the ice acted like the ocean and its skin temperature varied only slightly over the day.

Figure 10 shows the diurnal variation of CRF for the domain. SWCRF (figure 10a) reaches its absolute greatest values around 0700 and 1900 LT as a consequence of the cloud diurnal variability, the solar zenith angle, and the cloud albedos. Even as the cloud cover and μ_o increase toward local noon in the morning, the decreasing cloud albedo reduces the amount of reflected SW radiation. The cloud amount maximum is reflected in the inflection of the curves near 1100 LT during each month. The absolute minimums occur during early afternoon and around midnight. In the latter case, the sun angle primarily responsible, while the reduced cloud amount determines the mid-afternoon absolute minimum. LWCRF (figure 10b) is extremely flat, except during June. Thus, the diurnal variability in M_{lw} (figure 9) during May and July was due to the lack of a variation in mean cloud temperature. The 1 Wm^{-2} dip in LWCRF during June suggests either a slight decrease in the coverage by high clouds or that the clouds forming before noon were warmer than the surface. Net cloud forcing (figure 10c) mimics SWCRF because LWCRF lacked any substantial variability. NETCRF is negative throughout the entire day for all 3 months, a phenomenon that is probably confined only to the polar regions.

4. DISCUSSION

a. Error sources

The determination of radiative fluxes from satellite narrowband radiances is affected by many sources of uncertainty. The calibration of the narrowband instruments used to develop and apply the broadband conversion formulae must be consistent to eliminate bias. The bidirectional reflectance or limb-darkening models used to convert the radiances to flux are the single greatest error source because of the highly variable nature of the radiance anisotropy. Misclassification of the scene can affect the selection of the anisotropic correction models and the average clear or cloudy flux. If either value is biased, the net cloud radiative forcing will also be biased. The conversion of narrowband data to broadband fluxes also has significant uncertainties that can significantly affect the instantaneous values, while being less significant for monthly averages. Assessing each of these uncertainties individually and combining them to obtain a single error for each flux is an uncertain task in itself. Comparisons with other estimates or measurements of the radiation fields may be a more reasonable approach to assessing the quality of the derived fluxes.

b. Comparisons with surface data

The SW albedos derived the AVHRR data are compared in figure 11 with albedos computed with the FL and *Streamer* models using coincident surface albedos in clear skies. The satellite-derived albedos are generally greater than the FL results for the brightest scenes, while the surface data yield greater values for the middle range of albedos. *Streamer* gives slightly better agreement for the mid-range albedos and mostly larger values for the higher albedos. For these 13 data points, the mean differences between the satellite and model-calculated clear-sky albedos are -0.011 and –0.016 for the FL and *Streamer*, respectively. The corresponding standard deviations are 0.038 and 0.035.

The model-based overestimates of the TOA albedo relative to the satellite results may be due to a variety of errors in either the measurements or in the model calculations. Downwelling diffuse SW radiation is typically underestimated with pyranometers due to radiative cooling of the instrument [e.g., *Kato et al.* 1997]. Thus, the surface albedo may be overestimated with a subsequent overestimation of the TOA albedo. The FL-calculated downwelling SW flux exceeds the Eppley-observed value by nearly 10%. Some of this discrepancy may be due to differences in the spectral range, but it is likely that the diffuse radiation problem is affecting the observations. The true anisotropy in the reflectance field may differ from the values used in the albedo calculations. Because the satellite views the area from different angles during each overpass, this type of error should be a random-like effect and would tend to average out over several overpasses. Similarly, there are some random errors associated with the narrowband-to-broadband albedo conversion and variation within the satellite pixels used to compute the means for each comparison. The standard error of the regression-fit in figure 2 is nearly identical to the standard deviations in the model-observation comparison. The SHEBA surface albedo may not necessarily represent the area viewed by the satellite. A random error would result from the differences between the actual and assumed aerosols in the calculations. If they were systematically under- or overestimated, a bias in TOA albedo would occur. Another potential source of bias would be errors in the pyranometer calibrations. Given all of these error sources, the results plotted in figure 11 are quite reasonable. The random errors are no larger than expected and the mean differences are consistent with an underestimate of the diffuse radiation at the surface.

The clear-sky LW fluxes computed with the models are well correlated with the satellite-derived values (figure 12) with minimal difference between the model results. The *Streamer*-computed LW fluxes are 2.6 $\pm$ 3.3 Wm^{-2} greater than the AVHRR results, while the FL fluxes are 3.7 $\pm$ 2.6 Wm^{-2} greater than the satellite data. The opposite differences are seen in the computed downwelling LW fluxes at the surface in figure 13. The *Streamer* values are consistently less than the observed values with a mean difference of 6.9 Wm^{-2}, while the FL values average 6.3 Wm^{-2} less than the Eppley values. The up-and downwelling differences suggest that both models produce insignificantly different results. Thus, only the FL is used for the remainder of this study.

The opposing differences between the calculated and observed fluxes at the TOA and the surface suggest that the atmosphere may be moister than the indicated by the radiosondes. Normalizing the model results to the surface measurements would account for any errors in the moisture profile. Thus, the humidity at each level was incrementally increased or decreased to bring the FL results into agreement with the surface data. Using the resulting humidity profile to compute the TOA fluxes reduces the mean TOA LW flux difference to 0.5 Wm^{-2}. This 3.6 Wm^{-2} decrease in M_{lw}(TOA) for a 6.3 Wm^{-2} increase in the downwelling flux indicates that the atmosphere accounts for about 50% of the TOA LW flux for the summertime Arctic. Because it is based on model calculations that match the surface observations, it is concluded that the adjustment approach is probably a better way to compare the surface and TOA fluxes.

c. Comparisons with aircraft data

The aircraft data were taken over a variety of backgrounds including ice, snow, open water, and clouds over tundra. Figure 14 shows the comparison of the AVHRR albedos with the adjusted May and July C-130 Eppley and RAMS data. The AVHRR albedos are generally greater than their Eppley counterparts with no apparent differences for the dark or bright scenes as in figure 11. The mean difference between the AVHRR and Eppley albedos is 0.021 with a standard deviation of 0.037. Conversely, the RAMS albedos are typically a bit larger than the AVHRR values with no scene dependence. The mean difference is –0.006 $\pm$ 0.029. This latter random error is even smaller than the regression error in the AVHRR-based broadband albedos.

The albedos are subject to the same type of errors discussed for the surface comparisons. However, uncertainties in the model atmosphere have much less impact because most of the moisture and aerosols are below the aircraft. Use of several different Arctic atmospheres introduced errors no greater than 0.003 in the derived TOA albedos. The variety of scenes should also reduce the anisotropic correction error for the satellite data. Much of the error should depend on calibration of the radiometers. The Eppley radiometers are nominally accurate to within ~10 Wm^{-2} which would translate to an albedo error of 0.016 for the dataset in figure 14. However, they still require calibration maintenance when used on the aircraft. It is not clear how the Eppley calibrations were performed. The RAMS instruments were calibrated before and after each flight. Before each flight, a new set of calibrated instruments was installed on the aircraft to eliminate instrument-related drift and biases in the dataset. While the good agreement between the RAMS and AVHRR results may be fortuitous, it falls between the albedo differences found for the surface and C-130 Eppley results. Accounting for all of the comparisons, it is concluded that the mean albedos derived with the NOAA-12 and 14 AVHRR data are accurate to within 0.0 $\pm$ 0.015 and the instantaneous results have a one standard-deviation uncertainty of 7%. These results also confirm that the 1986 albedo correlations in figure 2 are applicable to the FIRE ACE period and may be accurate for other summertime periods within the domain.

Figure 15 plots the TOA-adjusted LW fluxes from the July Eppley data with the coincident AVHRR values. The two quantities are well correlated with a squared linear correlation coefficient of 0.78 and a mean difference of -0.1 Wm^{-2} with a standard deviation of 4.6 Wm^{-2} or 1.9%. Although this plot consists of only 10 data points, the small variance suggests that the mean difference is accurate to within 1 Wm^{-2} if a normal distribution of differences is assumed. The standard deviation is less than that found for the original regression between ERBE and AVHRR. The agreement is much like that found for the 13 clear-sky cases over the SHEBA when the model calculations were forced to agree with the surface data by altering the soundings. While such changes may introduce additional errors, they normalize the model to the aircraft (surface) instruments. Thus, nominally the difference between the satellite and modeled LW fluxes should be due to calibration errors and the anisotropic corrections for the AVHRR data. In this case, the agreement is remarkable and, together with the surface-based comparisons, it provides a high degree of confidence in the AVHRR-derived LW fluxes for the FIRE ACE period. It is concluded that the mean AVHRR LW flux is unbiased at the 1 Wm^{-2} level.

d. Climatology

The mean TOA radiative quantities for the FIRE ACE domain were computed using the ERBE-derived values for the period 1985-1988 for the area encompassed by 72.5 - 80.0°N and 150°-180°W. Table 2 summarizes the ERBE results for each month. The values derived during FIRE ACE are within the ERBE ranges for June and July. The mean May albedo during FIRE

ACE is 0.02 greater than the previously observed maximum albedo for the month, while the LW flux is the same as the previous maximum. If the correction from *Thomas et al.* [1995] were applied to the ERBE LW means, the range would shift upward by ~6 to 8 Wm^{-2} and the FIRE ACE values would still be within the historical range. Similarly, the net fluxes for the period are within the ERBE ranges except for May. The LW correction would not change that comparison. Thus, except for the May albedo, it may be concluded that the TOA radiation fields during FIRE ACE were not particularly extraordinary. The clear-sky data were not available for ERBE because of scene identification problems.

Ii is difficult to compare the present values to pervious results because of the limited domain used here. Earlier estimates are computed for a particular latitude or for nearly the entire Arctic Ocean. Missing clear-sky data precludes a direct comparison with the ERBE data. The LWCRF values in Table 1 are similar to the results of *Curry and Ebert* [1992] for 80°N, but are 5-10 Wm^{-2} less than computed by *Schweiger and Key* [1994] for all ocean areas north of 62.5°N. The SWCRF values are also about half of those calculated by *Schweiger and Key* [1994] for all 3 months and by *Curry and Ebert* [1992] for June and July. During May, the FIRE ACE SWCRF agrees with the latter results. The comparisons are virtually the same for the NETCRF. *Rossow and Zhang* [1995] obtain NETCRF values very close to the current results at 80°N latitude using ISCCP C2 data as reported by *Curry et al.* [1996]. The reasons for the agreement are not clear because the ISCCP C2 cloud amounts are considerably less than those obtained from the FIRE ACE data. Differences in the *Rossow and Zhang* [1995] LWCRF and SWCRF values may be canceling each other resulting in mean NETCRF fluxes that are close to the current results. The *Rossow and Zhang* [1995] data would need to be explored in more detail to resolve the apparent discrepancy between cloud amount and NETCRF. Nevertheless, the current results show that for this spring-to-summer period, the clouds in this domain cause a reduction in the amount radiative energy available to the Earth-atmosphere system. Conclusions about the surface radiative forcing will require analyses of the data taken at the SHEBA site.

e. Diurnal variability

The diurnal cycles observed in the hourly means are not particularly strong but appear to be significant with a peak in LW flux near local noon. To better understand these data, the SHEBA Eppley data were examined for a diunral variation in the surface upwelling flux. Figure 16 shows M_{lw}(TOA) and M_{lw}(SFC) for the SHEBA site during May 23-25, 1998, where SFC refers to the surface. The average diurnal range in M_{lw}(SFC) is ~ 35 Wm^{-2} while the corresponding M_{lw}(TOA) range is only 15 Wm^{-2}. The latter value may be reduced by the lack of samples near the minimum time. However, it appears that the M_{lw}(TOA) is not changing as rapidly as the M_{lw}(SFC) early in the morning. Thus, 15 Wm^{-2} may be a realistic estimate for the diurnal range in M_{lw}(TOA). These two daily realizations of the diurnal cycle are much greater than expected from the monthly hourly means. This result suggests that the interpolation process for deriving the monthly means may artificially reduce the diurnal amplitude of M_{lw}(TOA) for clear skies. However, it has minimal effect on the monthly clear-sky LW flux and LWCRF. A straight average of the M_{lw} for all observed clear-sky cases differs by less than 1 Wm^{-2} from the interpolated averaging result.

Examination of the few clear-sky days during June and July show a much reduced diurnal amplitude suggesting that the melt ponds are absorbing the solar radiation throughout the bulk of the melt pond with a gradual increase in the skin temperature of the ponds. The lack of a significant diurnal cycle is similar to the response of the ocean to solar absorption. During May, the larger diurnal range suggests that a thin surface layer is heating and melting, because the radiation is not penetrating the surface as much as it does later in the season when ponds are present. The diminished diurnal amplitude of M_{lw}(TOA) compared to that of M_{lw}(SFC) is consistent with the relative contribution of the atmosphere to M_{lw}(TOA). As shown in earlier calculations, the atmosphere accounts for about 50% of the TOA LW flux. Therefore, the diurnal amplitude in M_{lw}(TOA) should be roughly half of M_{lw}(SFC) as seen in figure 16.

6. CONCLUDING REMARKS

The results presented here show a negative cloud forcing at the TOA during late spring and early summer over the greater SHEBA domain. The small contrast between clear and cloudy scenes found during May for both shortwave and longwave radiation gives way to a more substantial shortwave forcing during July. The clouds are a dominant feature, covering an average of 70 - 80% of the domain; but because they radiate at nearly the same mean temperature as the surface, they only slightly reduce the loss of longwave radiation to space. The comparable radiating temperatures of the clouds and the surface suggest that much of the surface-emitted radiation is returned by the clouds. Thus, the cloud radiative forcing at the surface may be significantly different than that at the TOA.

A surprising finding of this study relates to the diurnal variation in the surface-emitted longwave radiation. While the snow is frozen, the surface radiation cycle is similar to that over land. Under clear skies, the surface heating varies sinusoidally with a maximum near noon. Without a sunset, however, the surface does not experience the exponential cooling observed at other latitudes over land. As the summer progresses, the Arctic surface behaves more like the ocean in that a small diurnal signal occurs, but its phase is more difficult to discern because of a relatively large noise in the small signal. This change in the diurnal cycle from more land-like to more ocean-like behavior suggests that a different approach is needed for modeling the diurnal variation of clear-sky longwave flux for snow-covered surfaces for radiation budget monitoring. Current approaches assume a linear variation like that used over ocean. A more sinusoidal interpolation may be required to improve the accuracy of the satellite-derived radiation budgets in polar regions.

A complete, accurate radiative depiction of the Arctic atmosphere is closer to realization than before FIRE ACE because of the excellent agreement found between the satellite and model-adjusted fluxes. The accuracy of the AVHRR-derived fluxes is within the expected uncertainties for both the satellite-model and ERBE regression datasets. Thus, they can be used reliably with the surface datasets. Using SHEBA radar data to define the locations of the clouds, together with refined application of the satellite data to determine the cloud optical properties and the surface radiometer measurements to determine the surface fluxes, will enable the development of a three-dimensional radiation profile of the troposphere within the SHEBA domain. In situ FIRE aircraft data, however, will be needed to aid the refinement of techniques for deriving cloud optical depth from satellite data over the Arctic. Methods based on currently available satellite instruments tend to overestimate cloud optical depth due to the sensitivity of the retrievals in bright background, low contrast scenes [e.g., Dong et al 1999]. Because of this uncertainty, cloud optical depths were not derived for this study. Additional analyses will be needed to provide a comprehensive and reliable cloud optical depth dataset for this period.

This study has clearly demonstrated the capabilities for determining cloud and clear radiative fluxes over the Arctic during summer using carefully analyzed AVHRR with a regionally dependent narrowband-to-broadband regression formula. With the development of similar regression formulae for other seasons, it should be possible to provide detailed flux data over the Arctic for the entire SHEBA period using the AVHRR data. With the year-long SHEBA surface dataset, it should then be possible to accurately constrain the energy budget of the Arctic Ocean at the surface and at the top of the atmosphere for an entire annual cycle.

Acknowledgments.
Special thanks to Bill Smith, Jr., Mandy Khaiyer, Pat Heck, Kirk Ayers, Shalini Mayor, and Anthony Bucholtz for monitoring and collecting the data during FIRE ACE. This research was supported by the NASA Earth Sciences Enterprise Radiation Sciences Program FIRE Project and by the Environmental Sciences Division of the U.S. Department of Energy Interagency Agreement DE-AI02-97ER62341 as part of the Atmospheric Radiation Measurement (ARM) Program sponsored by the Office of Science, Office of Biological and Environmental Research, Environmental Sciences Division. The ship data were also obtained from the ARM Program and from the NSF-SHEBA program under agreement #OPP-9701730.

References

Bannehr, L. and V. Glover, Preprocessing of airborne pyranometer data. NCAR Technical Note *NCAR/TN-364+STR*, National Center for Atmospheric Research, Boulder, CO, 1991.

Barkstrom, B. R., E. Harrison, G. Smith, R. Green, J. Kibler, R. Cess, and the ERBE Science Team, Earth Radiation Budget Experiment (ERBE) archival and April 1985 results, *Bull. Am. Meteorol. Soc.*, **70**, 1254-1262, 1989.

Curry, J. A. and E. E. Ebert, Annual cycle of radiation fluxes over the Arctic Ocean: Sensitivity to cloud optical properties. *J. climate*, **5**, 1274-1280, 1992.

Curry, J. A., W. B. Rossow, D. Randall, and J. L. Schramm, Overview of Arctic cloud and radiation characteristics. *J. Climate*, **9**, 1731-1764, 1996.

Curry, J. A., P. Hobbs, M. D. King, D. Randall, P. Minnis, T. Uttal, G. A.. Isaac, J. Pinto, et al. FIRE Arctic Clouds Experiment. In press, *Bull. Am. Meteorol. Soc.*, 1999.

Doelling, D. R., L. Nguyen, W. L. Smith, Jr., and P. Minnis, Comparison of ARM GOES-derived broadband fluxes and albedos with broadband data from ARM-UAV, ScaRaB, and CERES. *Proc. 8th Ann. ARM Sci. Team Mtg.*, Tuscon, AZ, March 23-27, 201-205, 1998.

Dong, X., G.G. Mace, P. Minnis, and D.F. Young, Arctic stratus cloud properties and their effect on the surface radiation budget; Selected cases from FIRE ACE. Submitted to *J. Geophys. Res.*, this issue, 1999.

Fu, Q. and K. N. Liou, Parameterization of the radiative properties of cirrus clouds. *J. Atmos. Sci.* **50**, 2008-2025, 1993.

Gupta, S. K., A. C. Wilber, N. A. Ritchey, W. L. Darnell, F. G. Rose, and T. P. Charlock, Regrid Humidity and Temperature Fields (Subsystem 12.0) Clouds and the Earth's Radiant Energy System (CERES) algorithm theoretical basis document, Volume IV: Determination of surface and atmosphere fluxes and temporally and spatially averaged products (Subsystems 5-12)", *NASA RP 1376 Vol. 4*, pp. 163-172, 1995.

Harrison, E. F., P. Minnis, B. R. Barkstrom, V. Ramanathan, R. D. Cess, and G. G. Gibson, Seasonal variation of cloud radiative forcing derived from the Earth Radiation Budget experiment. *J. Geophys. Res.*, **95**, 18,687-18,703, 1990.

Kato, S., T. P. Ackerman, E. E. Clothiuax, J. H. Mather, G. G .Mace, M. L. Wesely, F. Murcray, and J. Michalsky, Uncertainties in modeled and measured clear-sky surface shortwave irradiances. *J. Geophys. Res.*, **102**, 25, 881-25,898, 1997.

Key, J. and A.J. Schweiger, Tools for atmospheric radiative transfer: Streamer and Fluxnet. Computers and Geosciences, **24**, 443-451, 1998.

Minnis, P., Doelling, C. Venkatesan, D. A. Spangenberg, L. Nguyen, R. Palikonda, T, Uttal, M. Shupe, and R. F. Arduini, Arctic cloud coverage during FIRE ACE derived from AVHRR data. Submitted to *J. Geophys. Res.*, this issue, 1999.

Minnis P. and E. F. Harrison, Diurnal variability of regional cloud and clear-sky radiative parameters derived from GOES data; Part I: Analysis method. *J Climate Appl. Meteorol.*, **23**, 1032-1052, 1984.

Minnis P., P. W. Heck, and D. F. Young, Inference of cirrus cloud properties using satellite-observed visible and infrared radiances. Part II: Verification of theoretical cirrus radiative properties. *J. Atmos. Sci.*, **50**, 1305-1322, 1993.

Minnis, P. and W. L. Smith, Jr., Cloud and radiative fields derived from GOES-8 during SUCCESS and the ARM-UAV Spring 1996 Flight Series. *Geophys. Res. Ltrs.*, **25**, 1113-1116, 1998.

Minnis, P., D. F. Young, and E. F. Harrison, Examination of the relationship between infrared window radiance and the total outgoing longwave flux using satellite data. *J. Climate*, **4**, 1114-1133, 1991.

Perovich, D. K., E. L. Andreas, J. A. Curry, H. Elken, C. W. Fairall, T. C. Grenfell, P. S. Guest, J. Intrieri, et al., Year on ice gives climate insights. *Eos*, **80**, 481-486, 1999.

Rossow, W. B. and R. A. Schiffer, Advances in understanding clouds from ISCCP. *Bull. Am. Meteorol. Soc.*, **80**, 2261-2287, 1999.

Rossow, W. B. and Y.-C. Zhang, Calculation of surface Rossow, W. B. and and top-of-atmosphere radiative fluxes from physical quantities based on ISCCP datasets. Part II: Validation and first results. *J. Geophys. Res.*, **100**, 1167-1197, 1995.

Schweiger, A. J. and J. R. Key, Arctic Ocean radiative fluxes and cloud forcing estimated from the ISCCP C2 cloud dataset, 1983-1990. *J. appl. Meteor.*, **33**, 948-963, 1994.

Spinhirne, J. D., Visible and near IR lidar backscatter observations on the GLOBE Pacific survey missions. *Proc. AMS 7th Symp. on Meteorol. Observations and Instrumentation*, New Orleans, LA, J261-J264.

Stokes, G. M. and S. E. Schwartz, The Atmospheric Radiation Measurement (ARM) Program: Programmatic background and design of the Cloud and Radiation Testbed. *Bull. Am. Meteorol. Soc.*, **75**, 1201-1221, 1994.

Suttles, J. T., R. N. Green, P. Minnis, G. L. Smith, W. F. Staylor, B. A. Wielicki, I. J. Walker, D. F. Young, V. R. Taylor, and L. L. Stowe, Angular radiation models for Earth-atmosphere system: Volume I - Shortwave radiation. *NASA RP 1184*, 144 pp., 1988.

Thomas, D., J. P. Duvel, and R. Kandel, Diurnal bias in calibration of broad-band radiance measurements from space. *IEEE Trans. Geosci. And Remote Sens.*, **33**, 670-683, 1995.

Valero, F. P. J., R. D. Cess, M. Zhang, S. K. Pope, A. Bucholtz, B. C. Bush, and J. Vitko, Jr., Absorption of solar radiation by clouds: Interpretations of colocated measurements. *J. Geophys. Res.*, **102**, 29,917-29,927, 1997.

Valero, F. P. J., P. Minnis, S. K. Pope, A. Bucholtz, B. C. Bush, D. R. Doelling, W. L. Smith, Jr., and X. Dong, The absorption of solar radiation by the atmosphere as determined using consistent satellite, aircraft, and surface data during the ARM Enhanced Short-Wave Experiment (ARESE). In press, *J. Geophys. Res.*, October, 1999.

Young, D. Y., P. Minnis, D. R. Doelling, G. G. Gibson and T. Wong, Temporal interpolation methods for the Clouds and the Earth's Radiant Energy System (CERES) Experiment. *Jour. Appl. Meteor.* **37**, 572-590, 1998.

Table 1. Mean radiation quantities from AVHRR for FIRE ACE for 72.5 - 80.0°N and 150 - 180°W.

Property	May			June			July		
	TOTAL	CLEAR	CRF	TOTAL	CLEAR	CRF	TOTAL	CLEAR	CRF
α_{SW}	0.695	0.642		0.592	0.523		0.509	0.424	
M_{SW}, Wm^{-2}	291.7	269.5	-23.2	298.0	263.6	-35.8	235.3	195.8	-40.3
M_{LW}, Wm^{-2}	217.8	225.0	7.2	225.6	234.9	9.6	228.8	237.5	9.1
M_{NET}, Wm^{-2}	-89.7	-74.6	-15.9	-20.0	5.1	-26.2	-2.1	28.7	-31.2

Table 2. Mean radiative properties from ERBE for 1985-1988 for 72.5 - 80.0°N and 150 - 180°W.

	May		June		July	
	mean	range	mean	range	mean	range
α_{SW}	0.66	0.64 - 0.68	0.60	0.57 - 0.62	0.53	0.50 - 0.56
M_{LW}, Wm^{-2}	207.2	207 - 217	224.2	218 - 225	226.8	216 - 235
M_{NET}, Wm^{-2}	-66.7	-64 - -72	-23.8	-16 - -33	-7.3	-1 - -10

FIGURE CAPTIONS

Figure 1. Example of the model computations of SW albedo profiles used to correct the aircraft albedos to the TOA.

Figure 2. Scatterplot and regression fits for matched NOAA-9 AVHRR VIS and ERBE SW albedos for May-July 1986 for 2.5° regions between 65 and 75°N and 135 and 170°W.

Figure 3. Same as figure 2 except for matched IR and LW fluxes.

Figure 4. NOAA-12 AVHRR visible image and scene identification, albedo, and LW flux maps at 1936 UTC, 19 May 1998 over the Arctic Ocean. SHEBA camp denoted by “S.”

Figure 5. Distribution of clear and total SW albedo for FIRE ACE during May, June, and July 1998. Mean position of SHEBA camp denoted by the small box.

Figure 6. Same as figure 5, except for clear and total LW flux.

Figure 7. Same as figure 5, except for mean SW, LW, and net CRF.

Figure 8. Diurnal variation of mean clear and total SW albedos during FIRE ACE. Also shown is the variation of μ_o during July.

Figure 9. Same as figure 8, except for LW fluxes only.

Figure 10. Same as figure 8, except for CRF only.

Figure 11. Comparison of clear-sky TOA albedos from model calculations using SHEBA tower surface albedos and from coincident AVHRR data during FIRE ACE.

Figure 12. Same as figure 11, except for clear-sky LW fluxes using SHEBA tower upwelling LW fluxes in the models.

Figure 13. Comparison of downwelling LW flux at the SHEBA site computed from models using radiosonde profiles and measured by uplooking Eppley pyregeometers during FIRE ACE.

Figure 14. Comparison of TOA albedos derived from AVHRR and from C-130 Eppley pyranometers and the RAMS TSBR radiometers during May and July 1998.

Figure 15. Comparison of TOA LW fluxes derived from AVHRR and C-130 Eppley pyregeometers during July 1998.

Figure 16. Diurnal variation of surface and TOA fluxes at the SHEBA camp for clear days May 23-25, 1998.

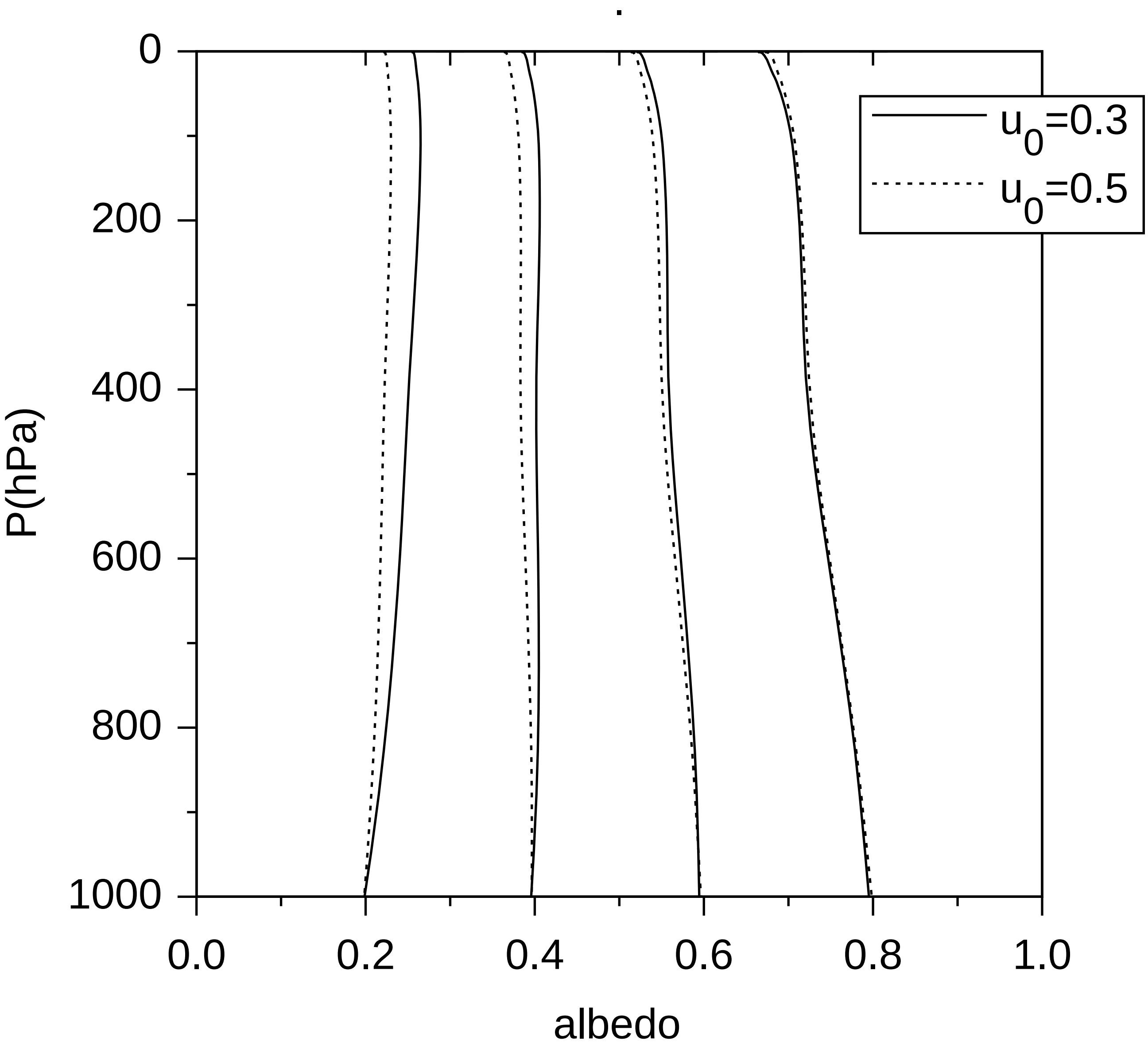

0
200
400
600
800
1000
P(hPa)
0.0
0.2
0.4
0.6
0.8
1.0
albedo
u0=0.3
u0=0.5

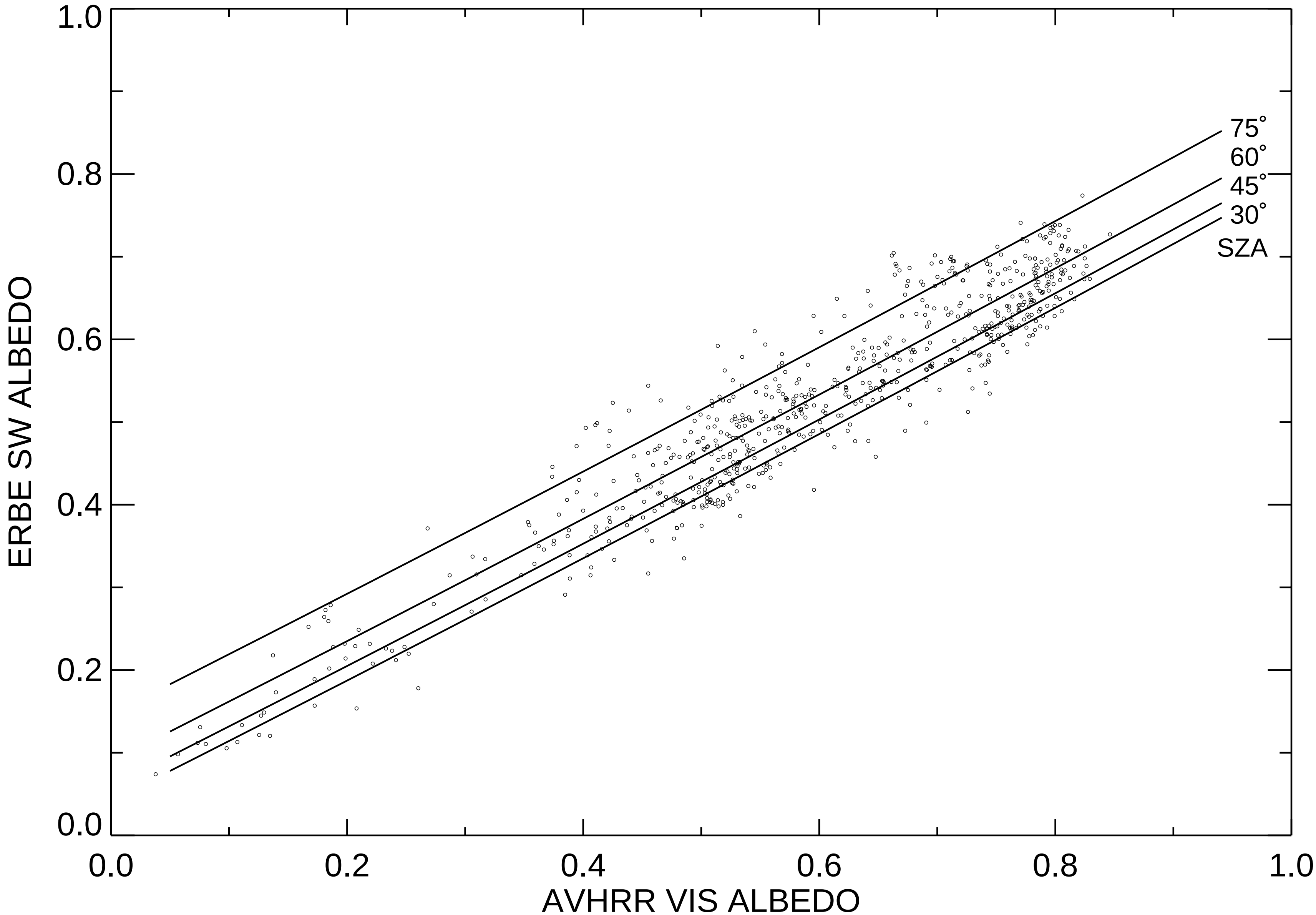
ERBE SW ALBEDO
AVHRR VIS ALBEDO
0.0
0.2
0.4
0.6
0.8
1.0
75°
60°
45°
30°
SZA

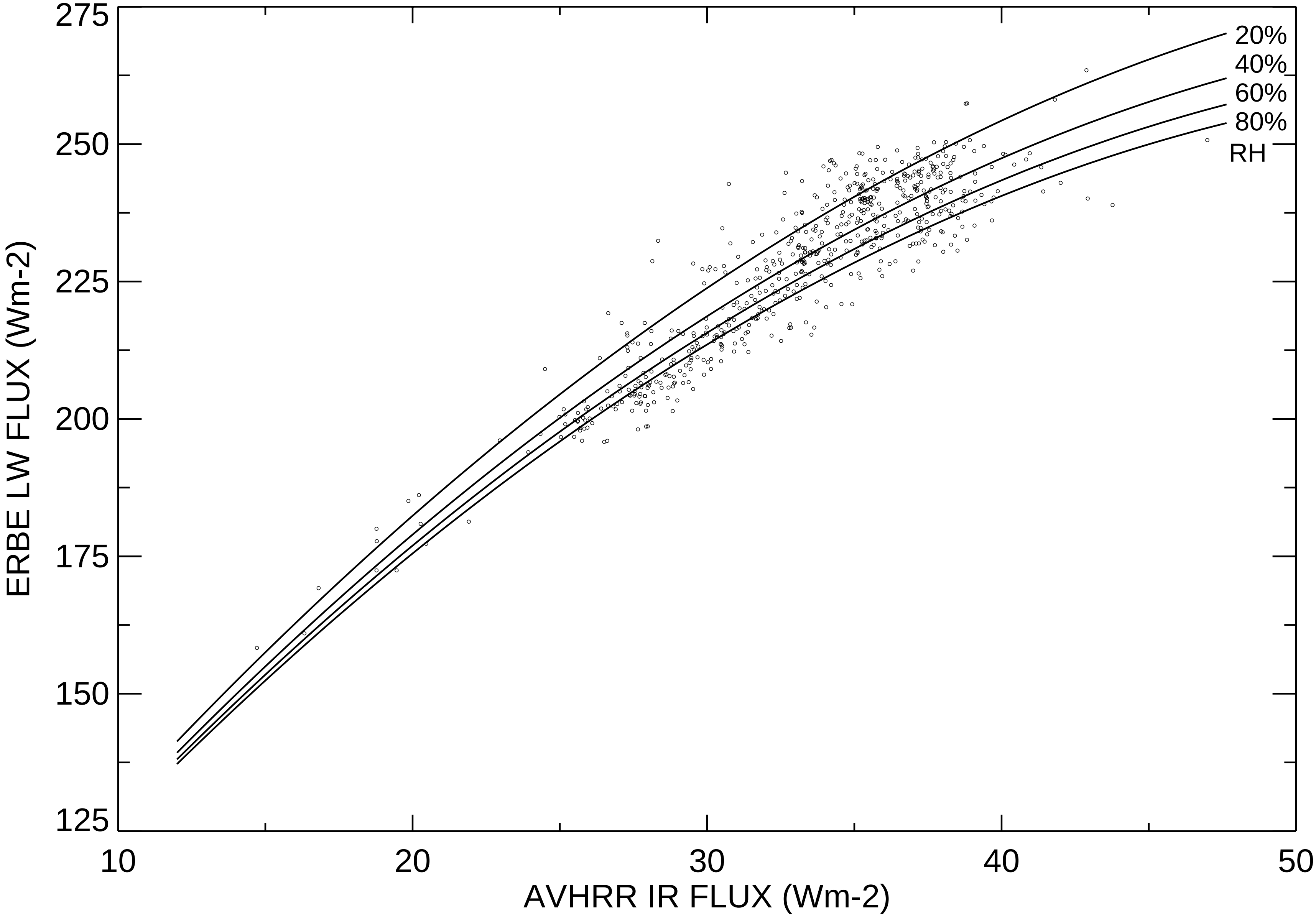

275
250
225
200
175
150
125
10
20
30
40
50
ERBE LW FLUX (Wm-2)
AVHRR IR FLUX (Wm-2)
20%
40%
60%
80%
RH

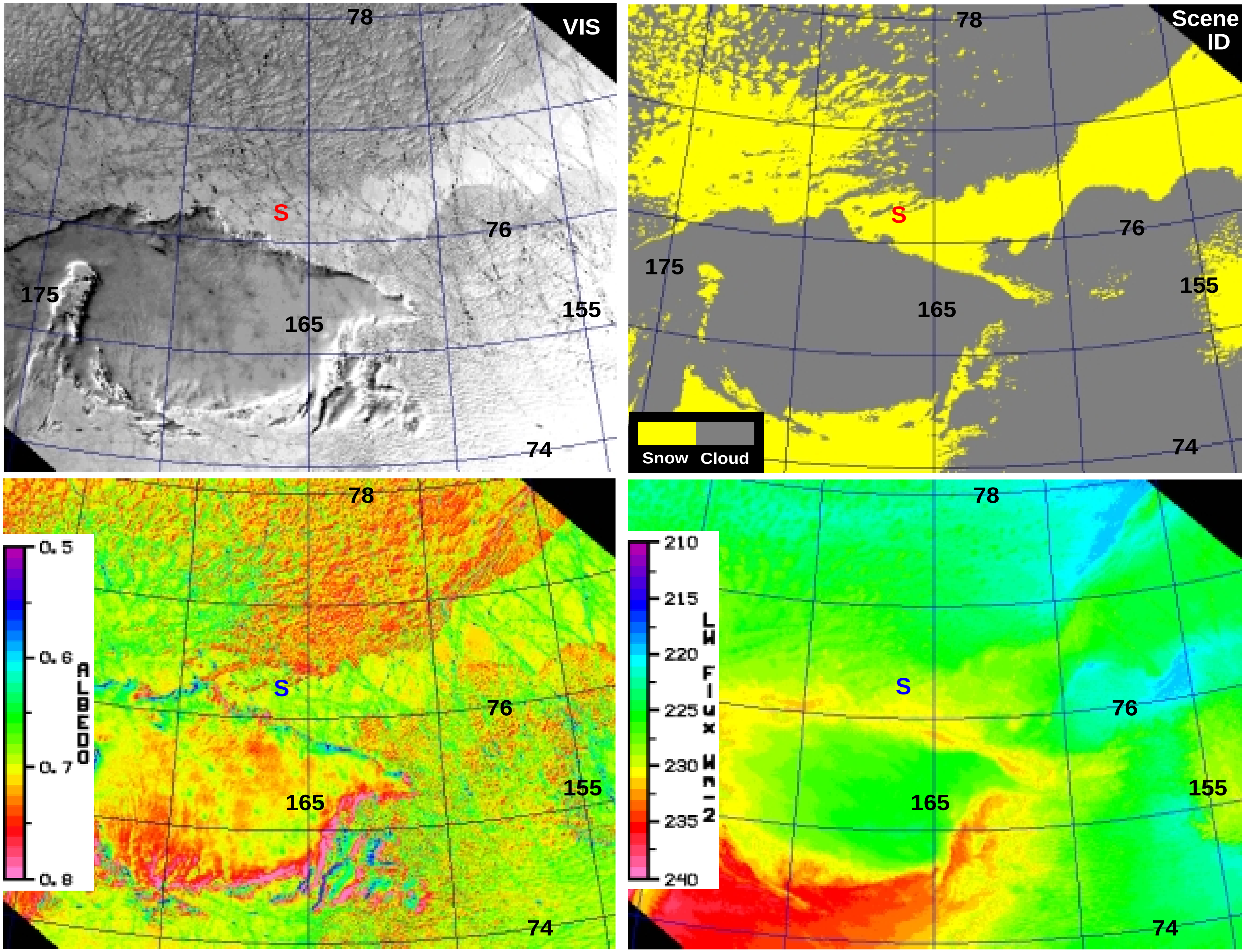
VIS
78
76
74
175
165
155
S
Scene ID
Snow
Cloud
0.5
0.6
0.7
0.8
ALBEDO
210
215
220
225
230
235
240
LW Flux Wm-2

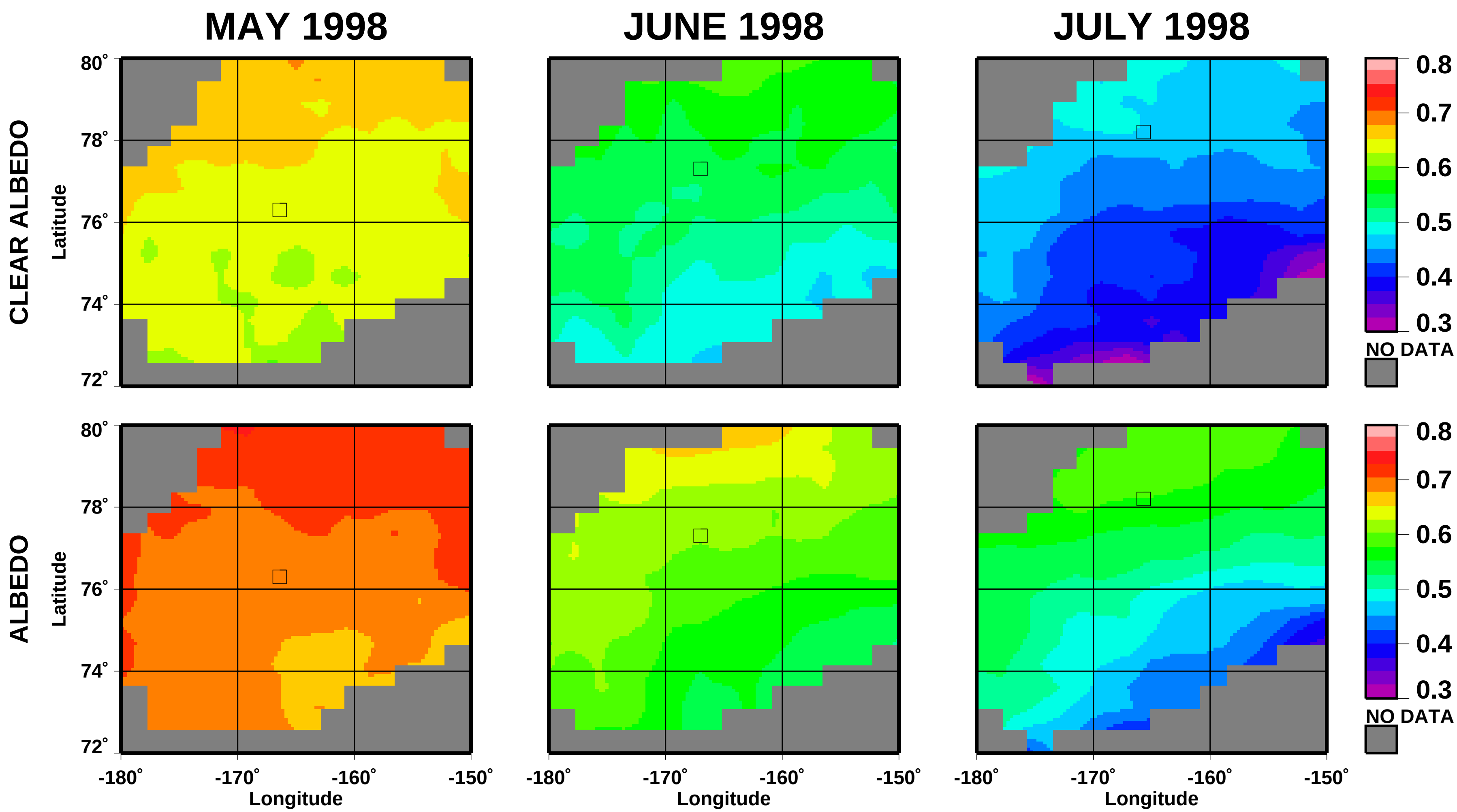

MAY 1998
JUNE 1998
JULY 1998
CLEAR ALBEDO
ALBEDO
Latitude
80°
78°
76°
74°
72°
-180°
-170°
-160°
-150°
Longitude
0.8
0.7
0.6
0.5
0.4
0.3
NO DATA

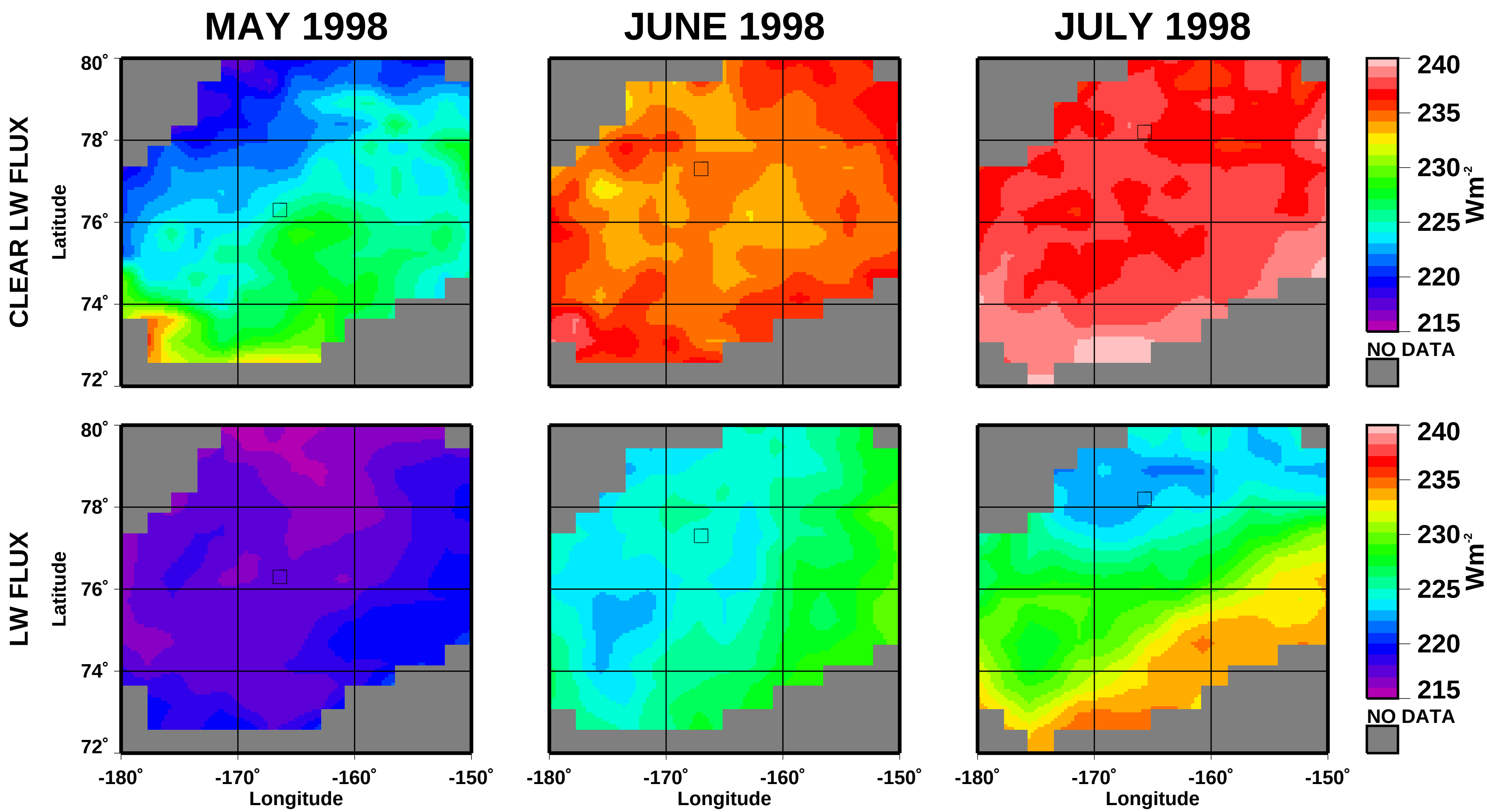
MAY 1998
JUNE 1998
JULY 1998
CLEAR LW FLUX
LW FLUX
Latitude
80°
78°
76°
74°
72°
-180°
-170°
-160°
-150°
Longitude
240
235
230
225
220
215
Wm-2
NO DATA

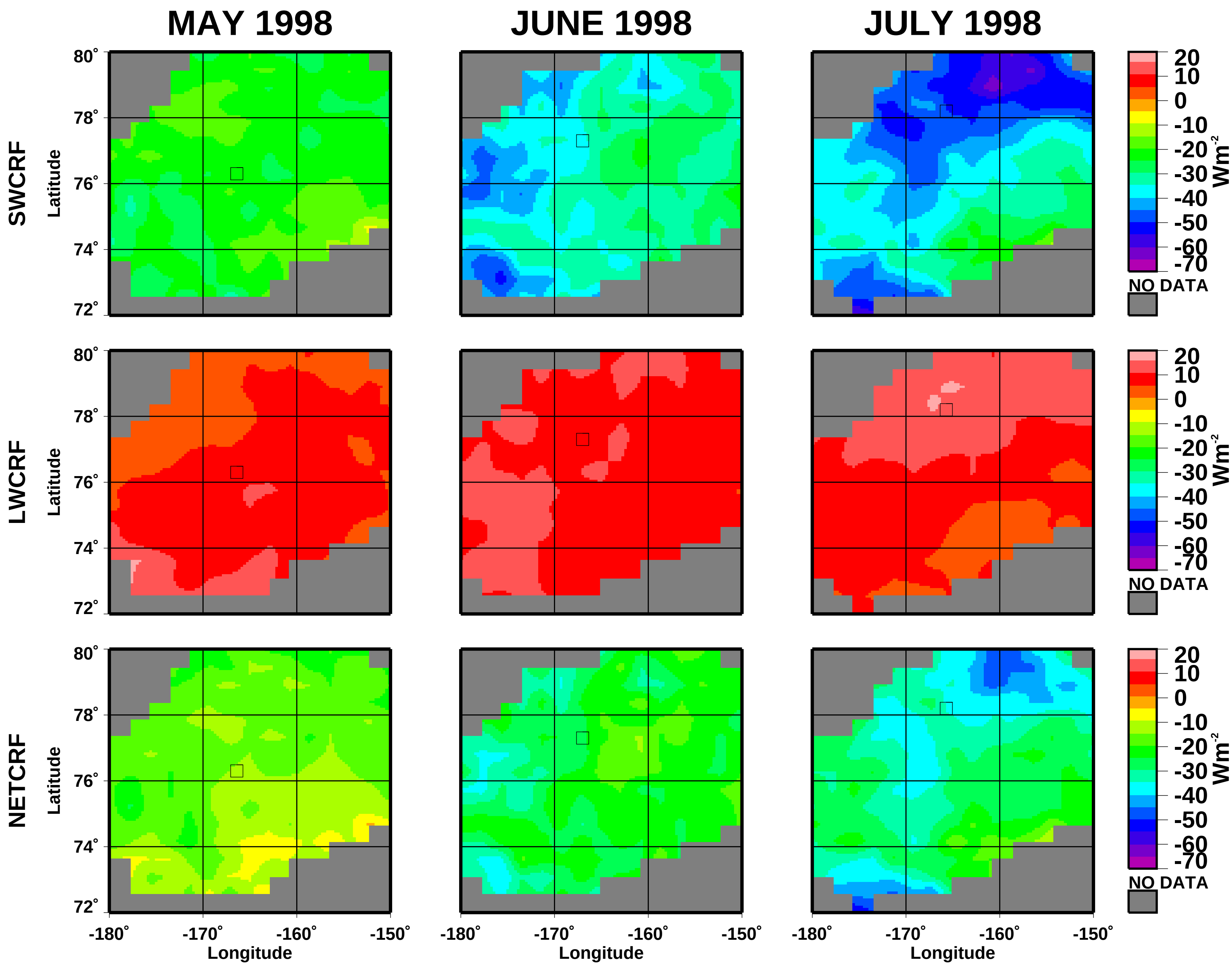

MAY 1998
JUNE 1998
JULY 1998
SWCRF
LWCRF
NETCRF
Latitude
80˚
78˚
76˚
74˚
72˚
-180˚
-170˚
-160˚
-150˚
Longitude
20
10
0
-10
-20
-30
-40
-50
-60
-70
Wm-2
NO DATA

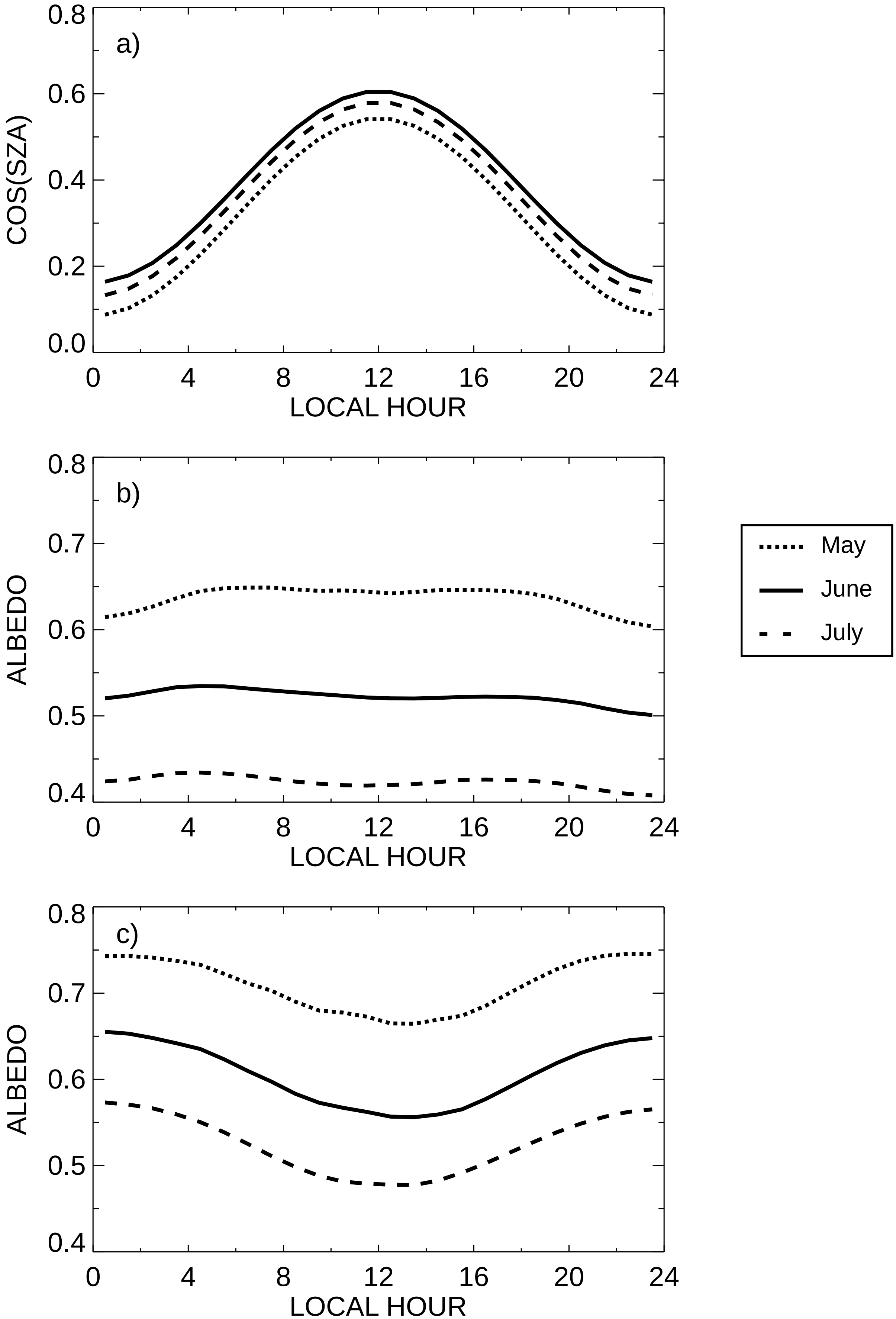
a)
COS(SZA)
LOCAL HOUR
b)
ALBEDO
LOCAL HOUR
c)
ALBEDO
LOCAL HOUR
May
June
July

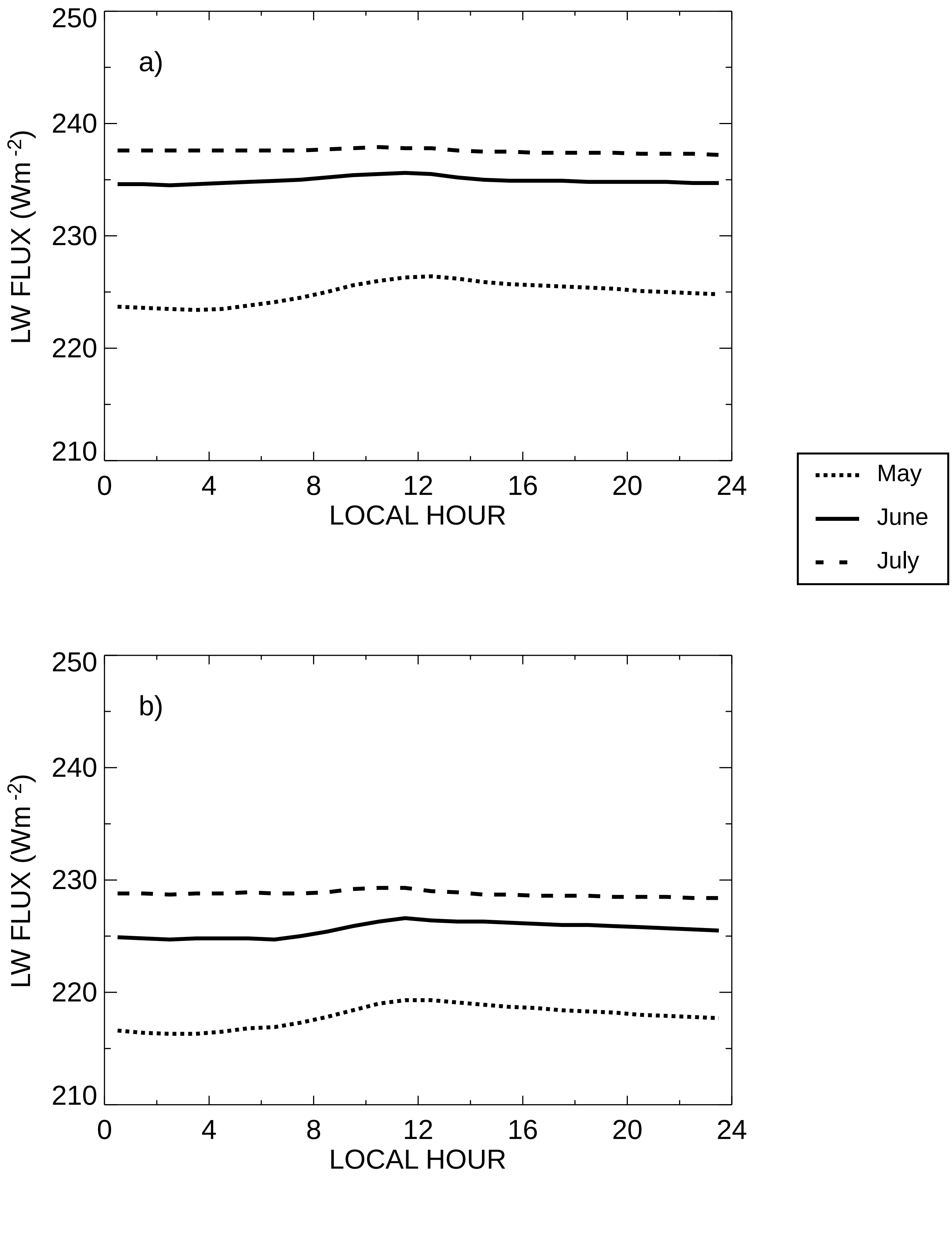

a)
b)
LW FLUX (Wm-2)
LOCAL HOUR
250
240
230
220
210
0
4
8
12
16
20
24
May
June
July

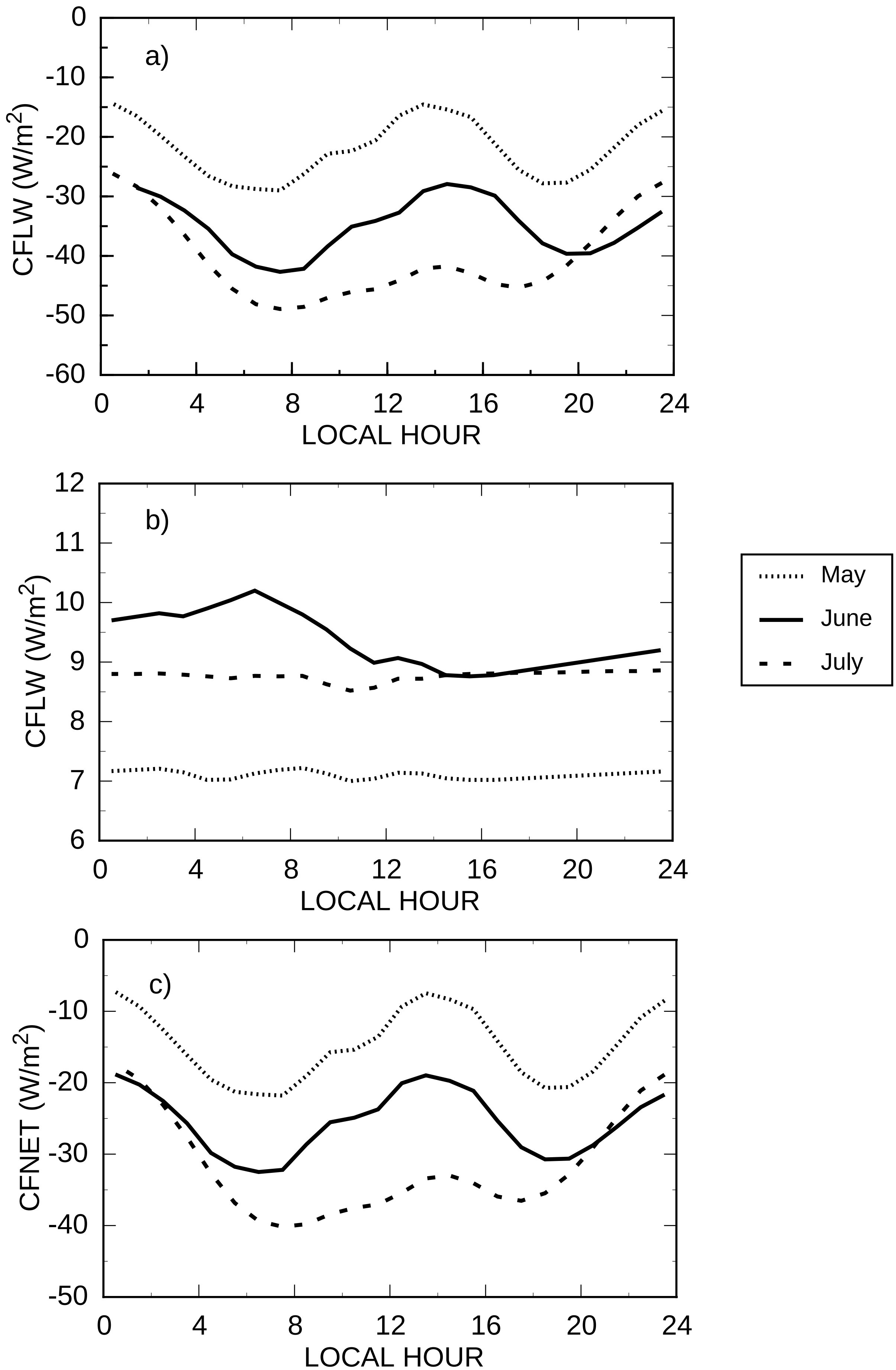
a)
CFLW (W/m2)
0
-10
-20
-30
-40
-50
-60
0
4
8
12
16
20
24
LOCAL HOUR
b)
CFLW (W/m2)
12
11
10
9
8
7
6
0
4
8
12
16
20
24
LOCAL HOUR
c)
CFNET (W/m2)
0
-10
-20
-30
-40
-50
0
4
8
12
16
20
24
LOCAL HOUR
May
June
July

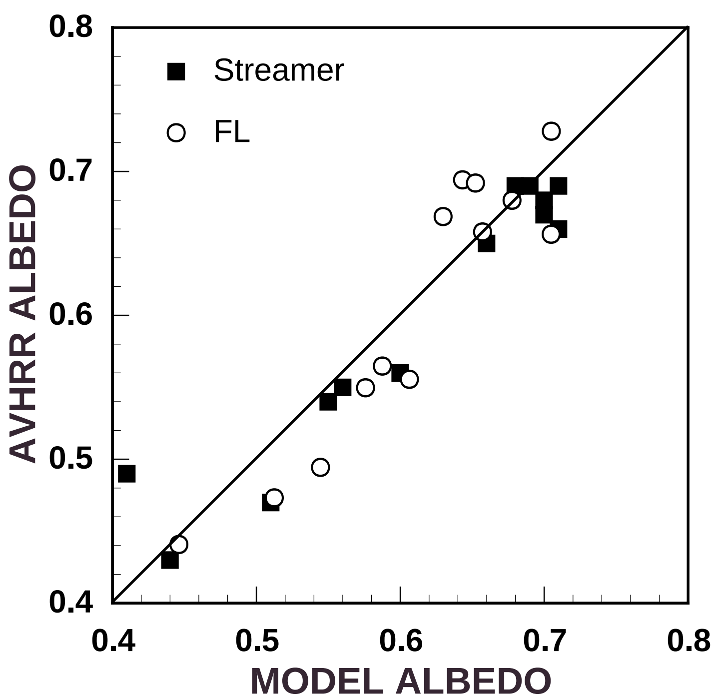

Streamer
FL
AVHRR ALBEDO
MODEL ALBEDO
0.4
0.5
0.6
0.7
0.8

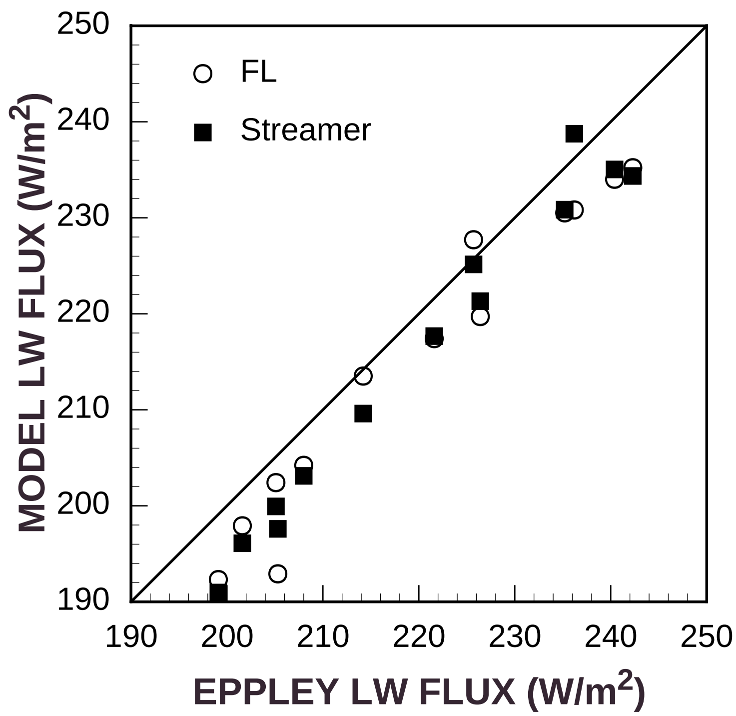
FL
Streamer
MODEL LW FLUX (W/m2)
EPPLEY LW FLUX (W/m2)
190
200
210
220
230
240
250

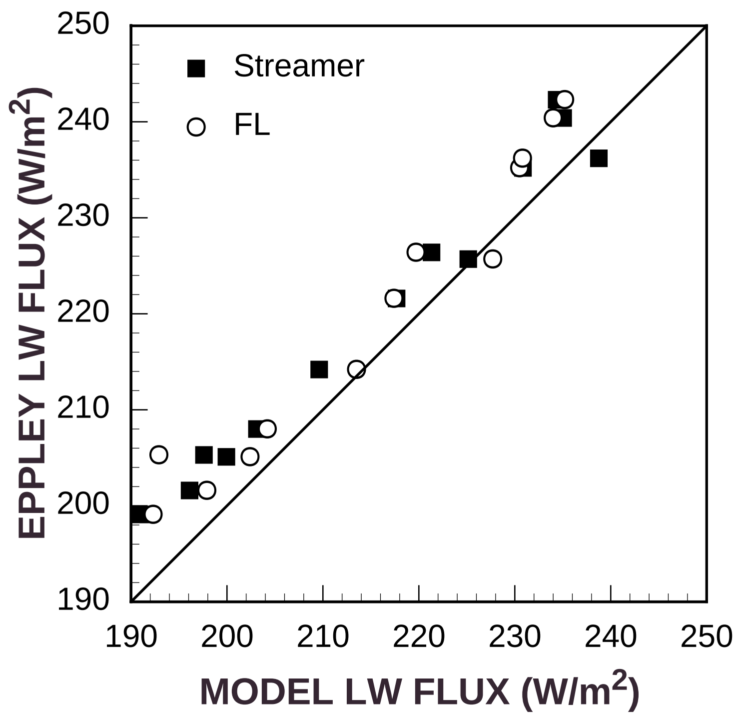

Streamer
FL
250
240
230
220
210
200
190
190
200
210
220
230
240
250
EPPLEY LW FLUX (W/m^2)
MODEL LW FLUX (W/m^2)

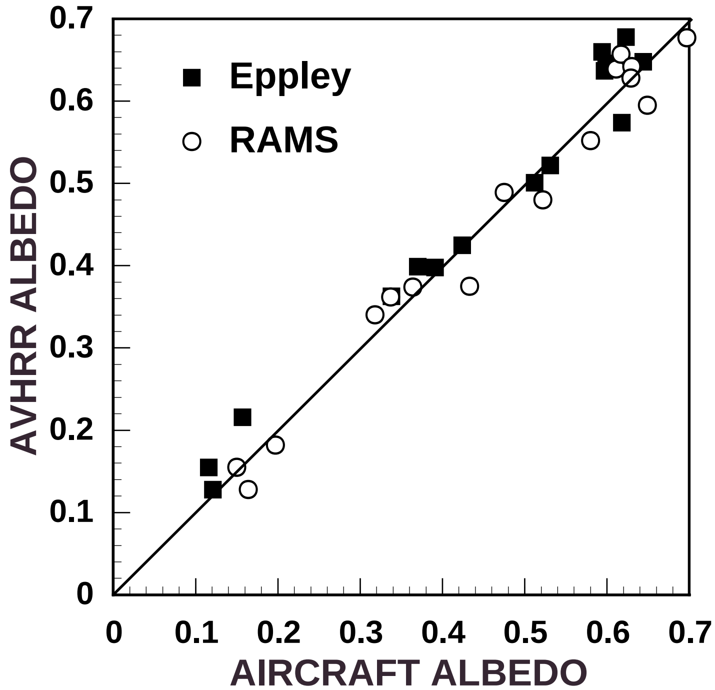

0.7
0.6
0.5
0.4
0.3
0.2
0.1
0
AVHRR ALBEDO
Eppley
RAMS
0
0.1
0.2
0.3
0.4
0.5
0.6
0.7
AIRCRAFT ALBEDO

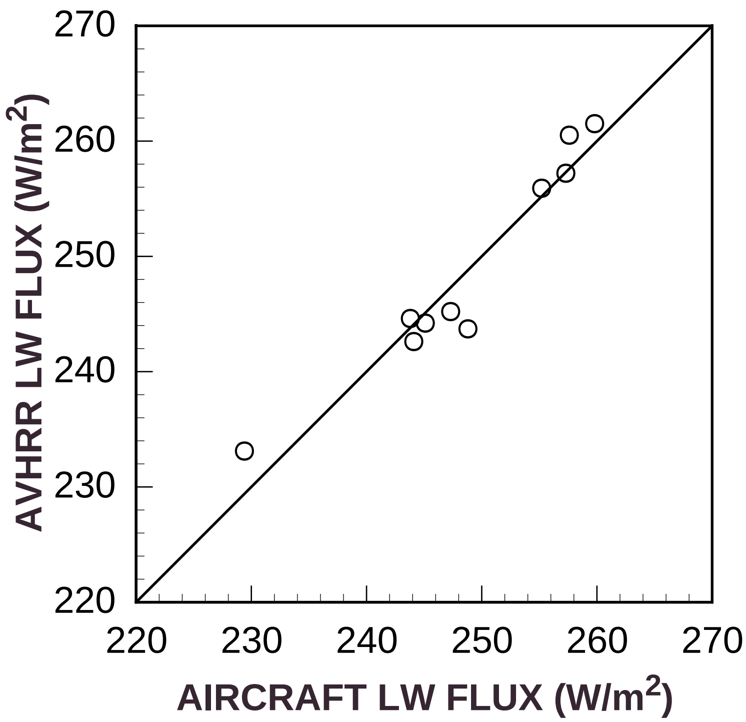
270
260
250
240
230
220
AVHRR LW FLUX (W/m2)
220
230
240
250
260
270
AIRCRAFT LW FLUX (W/m2)

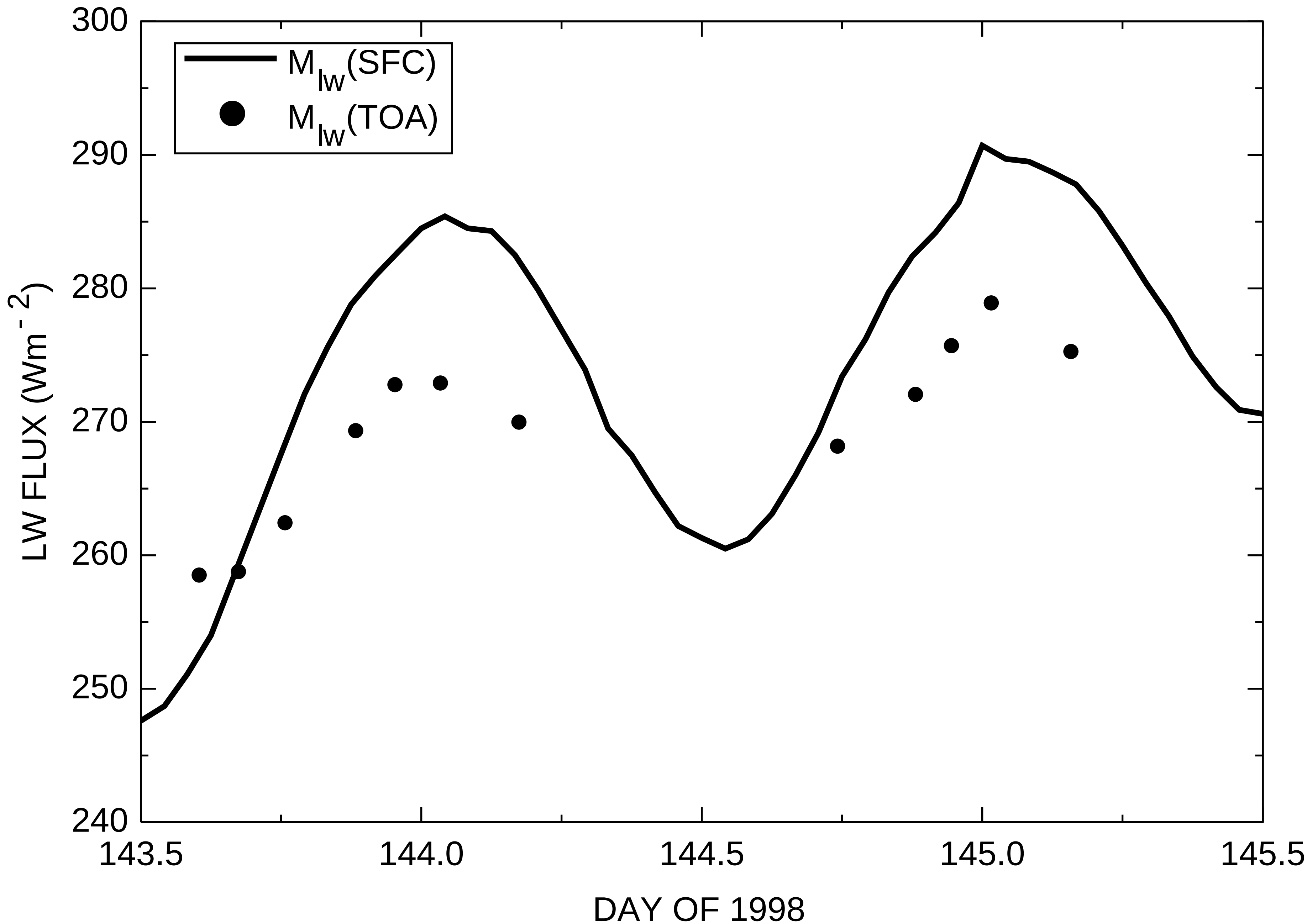

M_lw(SFC)
M_lw(TOA)
300
290
280
270
260
250
240
LW FLUX (Wm^-2)
143.5
144.0
144.5
145.0
145.5
DAY OF 1998